

Article

Organic Luminescent Sensor for Mercury(II) and Iron(III) Ions in Aqueous Solutions

Sofian Kanan ^{1,*} , Aysha Shabnam ¹, Ahmed A. Mohamed ²  and Imad A. Abu-Yousef ¹

¹ Department of Biology, Chemistry, and Environmental Sciences, American University of Sharjah, Sharjah P.O. Box 26666, United Arab Emirates; iabuyousef@aus.edu (I.A.A.-Y.)

² Department of Chemistry, University of Sharjah, Sharjah P.O. Box 27272, United Arab Emirates; ah.mohamed@sharjah.ac.ae

* Correspondence: skanan@aus.edu; Tel.: +971-6515-2409

Abstract: The substrate N¹, N³, N⁵-tris(2-hydroxyphenyl)benzene-1,3,5-tricarboxamide (**Sensor A**) was prepared in the reaction of 1,3,5-benzenetricarboxylic acid (trimesic acid) and *o*-aminophenol in ethanol. The prepared organic sensor fulfills the chemiluminescent requirements including a luminophore, spacer, and suitable binding receptor that distress the probe's luminescent features, providing selective and sensitive detection of mercury and iron ions in aqueous solutions. The sensor selectively detects mercury and iron ions in a water matrix containing various metal ions, including sodium, calcium, magnesium, zinc, and nickel. Strong and immediate binding was observed between mercury ions and the substrate at pH 7.0 with a binding affinity toward Hg²⁺ 9-fold higher than that observed for iron sensor binding affinity, which makes the substrate a distinctive luminescence sensor for mercury detection at ambient conditions. The sensor shows a linear response toward Hg²⁺ in the concentration range from 50 ppb to 100 ppm (2.0×10^{-8} to 4.2×10^{-5} M) with a limit of detection of 2 ppb (1.0×10^{-8} M). Further, **Sensor A** provides linear detection for iron ions in the range from 10 ppb to 1000 ppm (1.5×10^{-8} to 1.5×10^{-3} M). The measured adsorption capacity of **Sensor A** toward mercury ions ranged from 1.25 to 1.97 mg/g, and the removal efficiency from water samples reached 98.8% at pH 7.0. The data demonstrate that **Sensor A** is an excellent probe for detecting and removing mercury ions from water bodies.

Keywords: luminescent sensors; mercury ions; iron ions; binding affinity; selective detection; adsorption capacity



Citation: Kanan, S.; Shabnam, A.; Mohamed, A.A.; Abu-Yousef, I.A. Organic Luminescent Sensor for Mercury(II) and Iron(III) Ions in Aqueous Solutions. *Chemosensors* **2023**, *11*, 308. <https://doi.org/10.3390/chemosensors11050308>

Academic Editor: Chao Lu

Received: 23 April 2023

Revised: 17 May 2023

Accepted: 18 May 2023

Published: 20 May 2023



Copyright: © 2023 by the authors. Licensee MDPI, Basel, Switzerland. This article is an open access article distributed under the terms and conditions of the Creative Commons Attribution (CC BY) license (<https://creativecommons.org/licenses/by/4.0/>).

1. Introduction

Pollutants, especially heavy metals, deposited in ecological systems are a major concern due to their toxicity. Heavy metals are of great interest due to the role they play in environmental and biological systems. Compared to other organic pollutants, heavy metals are very stable substrates at ambient conditions, so they accumulate in soil and water bodies and thus are transported to humans and mammals through the food chain [1–4]. Most of the reported heavy metals receive great attention from environmental sectors and health agencies due to their harmful effect on humans and living environments even in very small concentrations. Specifically, studies showed that the presence of lead, cadmium, and mercury contaminants might damage many organs and tissues, including the brain, bone, and liver, and cause calcium metabolism disorders, leading to certain types of cancer [5–10]. Despite the harmful effects they inflict upon human health and the environment, these heavy metals are widely used in our daily life since they play a key role in many industries. For instance, mercury is deposited into the environment through various industrial actions including mining, coal combustion, metal smelter exhaust, and paper mills [11–13]. Combustion and industrial sources are significant for mercury emission into the environment, and most of the anthropogenic mercury emissions are associated with the burning

of fossil fuels, coal, and oil. In addition, being part of major industrial products of daily use including batteries, paper, latex paints, and electronics, mercury deposition into the environment is significant especially when no effective and direct recycling processes are applied. Mercury accumulates in the environment in three forms, and Hg^{2+} is the most widely spread.

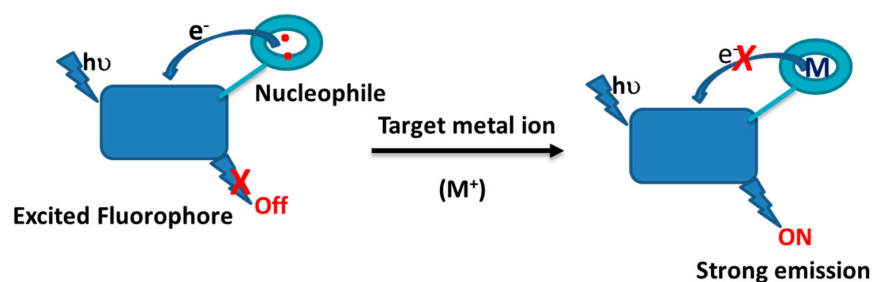
In contrast to mercury, iron is one of the major elements that is widely used in various industrial applications [14,15]. As an essential element, iron is a very important element to humans and other living organisms. Despite its importance in human health, iron content should be optimized; cases with deficient or saturated levels of iron are reported to cause function disorders, weak immunity, and lack of sleep [16–18]. As a result, high levels of iron contamination in drinking water pose health concerns, and thus the World Health Organization recommended that the iron (III) levels in drinking water be very low [19].

Given the high stability of heavy metals along with the direct and indirect effects they have on human health, there is a demand to selectively and sensitively detect their presence in both environmental and biological samples. Several instruments and methods were modified to detect and quantify mercury and other toxic metal ions in water bodies. The common techniques in use include atomic absorption spectrometry (AAS) [20,21], inductively coupled plasma techniques [22–24], and electrochemistry [25]. In some cases, these methods were modified and used along with various separation chromatographic methods including ion chromatography, gas chromatography, and high-performance liquid chromatography [26,27]. While these methods are very sensitive with a wide range of linearity, the high cost, long operation, and complicated sampling processes of such techniques increase the need to find simpler and faster methods that provide similar results in a shorter time. Recently, chemiluminescent sensors were modified to investigate organic and inorganic analytes in biological and environmental systems [28–30]. This provides a simple method to detect target molecules/ions with low detection limits over a short time. Importantly, luminescence-based sensors can be further designed to attain an “antenna” with a wide range of signaling when the analyte covalently binds to the luminescent probe, providing opportunities to monitor the concentrations of the target within a short time. This antenna can be observed through changes in the signal’s intensities, wavelength, lifetime, and chirality [28–32].

The photophysical properties of a fluorophore can be designed by establishing proton-, energy-, or electron-transfer processes that are sensitive toward the target molecules, including heavy metal ions. One of the most common strategies used to build luminescent devices is to facilitate the photoinduced electron transfer (PET) process that turns the emission *on or off* upon target analyte binding/interaction (see Scheme 1). Three major features must be present for designing a luminescent sensor: the luminophore, spacer, and receptor. When the target analyte binds to the receptor, an immediate change in the emission occurs where emission intensity may be enhanced or quenched, making “*off-on*” or “*on-off*” sensors, as illustrated in Scheme 1. Variations in the emission spectra may occur through various mechanisms including PET, ligand-to-metal charge transfer (LMCT), or metal-to-ligand charge transfer (MLCT) [30–34]. Several studies reported that the LMCT involves electronic transitions from the localized orbitals in the conjugated linker to a metal-centered orbital and is highly sensitive to the ionic size and the coordination geometry of the linker [30–37].

While several conjugated organic molecules were reported for metal ion detection at low concentration levels [30–37], the available fluorescent sensors that selectively detect mercury at ambient environmental conditions are limited. Much attention has been focused on porphyrin derivatives with strong fluorescent properties that are quenched upon the addition of mercury ions as *on-off* type sensors [38–40]. Additionally, most of the reported luminescent chemosensors lack selectivity and water solubility, which hinders their use in real environmental samples. In the present investigation, we synthesized $\text{N}^1, \text{N}^3, \text{N}^5$ -tris(2-hydroxyphenyl)benzene-1,3,5-tricarboxamide (**Sensor A**) that is tailored to three different suitable sites to capture metal ions by forming a five-membered ring between the linker and

the target metal ion of use. Both the orientation of the donor sites and the associated space are designed to covalently bind to Hg^{2+} . For the potential use of **Sensor A** for real water samples, we tested several water samples of environmental, tap, and deionized water. Since our goal was to find a selective and sensitive sensor for the detection of specific metal ions in water bodies, the photophysical properties of **Sensor A** toward various concentrations of metal ions, including Hg^{2+} , Mg^{2+} , Na^+ , Zn^{2+} , Ni^{2+} , Pb^{2+} , Fe^{3+} , and Ca^{2+} ions, were investigated in various aqueous solutions adjusted at three different pH values (pH 5, 7, and 10).



Scheme 1. Schematic illustration of luminescent sensors based on the fluorophore-receptor photoinduced electron transfer process.

2. Materials and Methods

All chemicals and reagents, including 1,3,5-benzenetricarboxylic acid (trimesic acid), *o*-aminophenol, iron (III) nitrate, mercury (II) nitrate, zinc nitrate, magnesium nitrate, sodium nitrate, nickel (II) nitrate, ethanol, and phosphate buffers, were purchased from Sigma-Aldrich and used without further purifications. In addition, 1000 ppm standard solutions were purchased from Sigma-Aldrich and used for quality control in this study. All solvents used were of analytical reagent grade, and the water used was double-distilled water. The metal ion solutions were prepared from their nitrate salts with specific metal concentrations calculated to represent the quencher concentrations.

UV-visible measurements were recorded on a single-beam UV-visible spectrophotometer (Cary 50 Conc) equipped with a xenon arc lamp. Fluorescence spectra were recorded using a Cary Eclipse Varian spectrophotometer equipped with a 150 W continuous xenon lamp along with a sensitive grating and PMT detector. The machine has a feature for surveying the excitation and emission profile of the fluorophore. Excitation and emission curves were recorded upon exposure to the selected emission and excitation wavelengths, respectively. Infrared spectra were recorded using the ABB Bomem MB3000 series combined with the intuitive Horizon MB FTIR software. NMR spectra were recorded on a Bruker 400 MHz. Finally, GC-MS was performed on a QP2010 Ultra gas chromatography/mass spectrometry (GC-MS) instrument (Shimadzu, Japan) using a 30 m RTX-1 capillary column. For the assessment, the injector and initial oven temperatures were set at 250 °C and 60 °C, respectively. Then, the column temperature was ramped at a rate of 7 °C/min to reach 320 °C and held constant for 20 min. The ion source and the interface temperatures of the mass detector were set at 240 °C and 280 °C, respectively.

2.1. Synthesis of Sensor A

Compound A was synthesized by a solvothermal process where trimesic acid (0.693 g, 3.3 mmol) and *o*-aminophenol (1.06 g, 9.9 mmol) were dissolved in ethanol (20 mL each). The trimesic acid solution was connected to reflux at 80 °C. When all the solid dissolved, the *o*-aminophenol solution was gradually added and continued under reflux for 6 h with continuous stirring where no starting materials remained, as depicted by thin layer chromatography. The red precipitate formed after slow cooling to room temperature and was filtered and crystallized from ethanol. The collected precipitate was dried in an oven at 80 °C for 2 h and then air-dried for 1 h before further use in this study. The material was characterized using UV-visible, luminescence, FTIR, and NMR spectroscopic techniques.

The reaction yield obtained was 93% with a high melting point of >300 °C. FTIR (KBr): ν (cm^{-1}) 3373, 1691, 1604, 1495, 1460, 1381, 1280, 1110, 928 cm^{-1} . Proton NMR (^1H NMR, 400 MHz, d_6 -DMSO) showed δ (ppm) 8.90 (s, 3H), 8.0 (s, 3H), 7.47 (d, 3H), 6.7–6.84 (d, 9H), 5.0 (s, 3H). The mass spectrum of the GC peak at 23 min showed a molecular ion peak at 483 amu with major fragments at 91, 129, 157, 253, 307, and 405 amu (see Figure S2).

2.2. Binding Studies

We relied on synchronous scan luminescence spectroscopy (SSLS) to monitor the changes associated with the fluorimetric and colorimetric features for detecting different metal ions in water samples. Solutions of **Sensor A** (30 ppm) were prepared in methanol:water, 10:90 *v:v*, solutions buffered at pH 5, 7, and 10 using phosphate buffers. Several concentrations of the tested analytes, including Zn^{2+} , Hg^{2+} , Mg^{2+} , Na^+ , Ca^{2+} , Ni^{2+} , and Fe^{3+} ions, were prepared from their nitrate salts with concentrations ranging from 0.5 to 1000 ppm. The initial luminescence intensity was recorded for a solution containing 2.75 mL of **Sensor A** diluted with water to a 3.0 mL total volume. The fluorescence intensity was monitored to reach stable emission; thus, maximum binding and quenching affinity was reached. Using a 100 ppm solution of the metal ion of interest, it was noticed that immediate responses occurred with iron and mercury ions, and no change in the emission profile occurred when other metal ions were used even after being monitored for 30 min. Even though the binding affinity occurred immediately, we followed the binding affinity for all tested various metal ion concentrations after 2 min intervals for a complete binding to be established. To ensure that the observed inhibition of the luminescence intensity is directed to the binding affinity between the sensor and the target metal ions, equal volumes of water (0.25 mL) were added to the organic sensor for an initial emission intensity that was used as F^0 .

2.3. Quantum Yield Analysis

Absorbance and luminescence spectra were recorded for known concentrations of Sensor A and fluorescein solutions in methanol. The fluorescence quantum yield for Sensor A (Φ_s) was determined by comparing the molar absorption coefficient, the wave number integration of fluorescent spectra between Sensor A and the standard solution as shown in Equation (1). One of the most common standards used is fluorescein which has a known Φ_{st} value of 0.85.

$$\Phi_s = \frac{(\text{Area})_s}{(\text{Area})_{st}} * \frac{(\text{Abs})_{st}}{(\text{Abs})_s} * \Phi_{st} \quad (1)$$

2.4. Equilibration Adsorption Measurements

To evaluate the adsorption of mercury ions on **Sensor A**, a 2 mL solution containing 6.0 mg of **Sensor A** was monitored upon adding various volumes of 50 ppm mercury ion solution at pH 7 for 10 min. The initial and the final equilibrium concentrations were determined from the emission intensity at 515 nm. The equilibrium adsorption capacity of mercury ions on **Sensor A** was then determined using Equation (2).

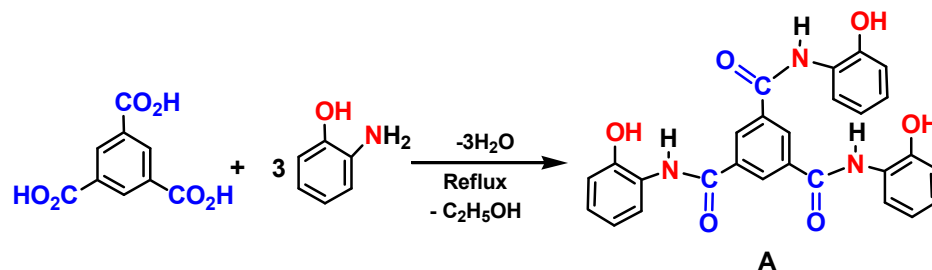
$$Q_{eqm} = (C_o - C_{eqm}) V/W \quad (2)$$

where Q_{eqm} is the equilibrium adsorption capacity, C_o is the initial concentration of the sensor, and C_{eqm} is the equilibrium concentration of the adsorbent. V and W represent the solution's volume and the mass of the adsorbent, respectively. Finally, the removal efficiency from the initial concentration, η %, was determined using Equation (3):

$$\eta \% = (C_o - C_{eqm})/C_o \times 100 \quad (3)$$

3. Results and Discussion

The luminescent **Sensor A** was prepared in a one-pot reaction of trimesic acid and *o*-aminophenol in a 1:3 mole ratio (Scheme 2). The product was crystallized from ethanol and dried at 100 °C for 1 h.



Scheme 2. The synthetic scheme for the preparation of **Sensor A**.

Figure 1 shows the excitation and emission spectra of **Sensor A** depicted at the indicated wavelengths. The compound also possesses strong excitation and emission profiles in UV and visible regions. The emission profile depends on the selected excitation wavelength. For instance, a strong emission appears at 571 nm upon excitation at 515 nm, whereas emissions were observed at 375 and 515 nm upon excitation at 325 nm. The excitation profile monitored at 572 nm also indicates bands at 512 and 325 nm aligned to the absorption bands depicted from the UV-Vis absorption spectrum. The obtained absorption and emission profiles are due to the high conjugation chain along with plausible $n-\pi^*$ transitions. Figure S1A shows a full-range 2D excitation–emission profile where the maximum luminescent features appear in the visible range from 500 to 700 nm. The appearance of the emission bands in the visible region corresponds to the presence of the extended conjugation of the designed fluorophore with the two aminophenol substrates via the possible formation of amide-imido tautomers in the solution that extends the conjugation to all fused rings (Scheme 3).

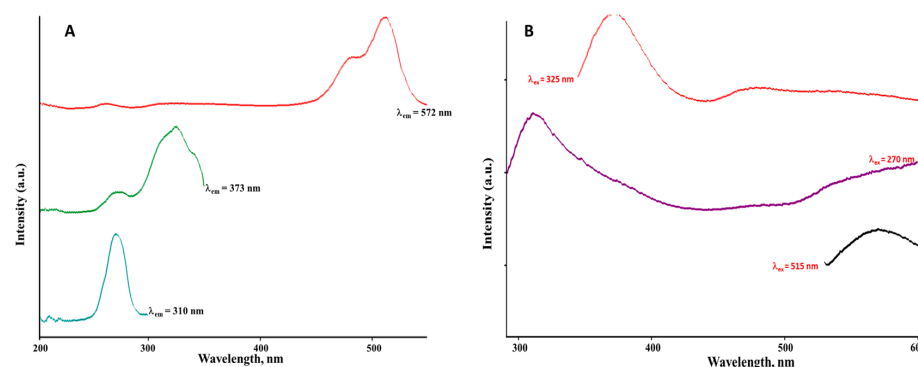
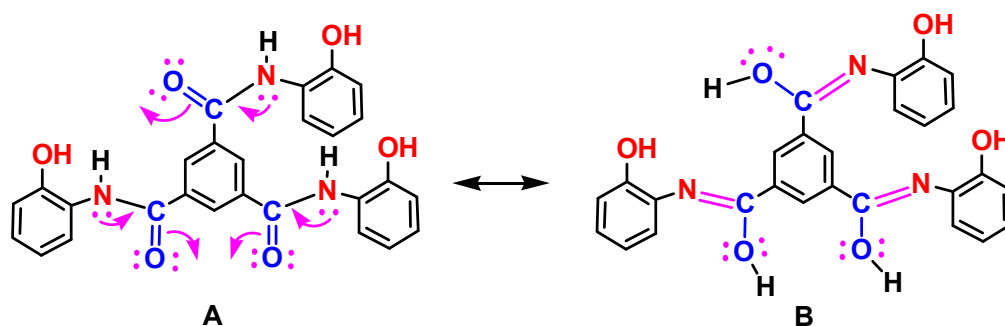


Figure 1. (A) Excitation spectra of **Sensor A** monitored at various emission wavelengths (λ_{em}) as labeled; (B) emission spectra of **Sensor A** monitored at the indicated excitation wavelengths (λ_{exc}).



Scheme 3. Plausible amide-imido tautomers of **Sensor A** in aqueous solution.

The selection of **Sensor A** for metal ion detection stems from the strong chain of conjugation that provides reasonable clear and strong fluorescence and absorption properties with a special molecular skeleton, with efficient binding sites for metal ions that cause a direct and sudden change in its luminescent features. Finally, the material is highly soluble in polar solvents, and thus the testing protocols can be applied to real environmental samples as illustrated herein. Given the broad features of the UV–visible absorption bands and the lack of well-defined emission bands due to the selected excitation wavelengths, we relied on synchronous scan luminescence spectroscopy (SLS) rather than ordinary emission or excitation spectra for monitoring the binding interaction with the target metal ions. This method involves recording the luminescence intensity while both the excitation and emission monochromators are varied at a constant wavelength difference ($\Delta\lambda$) [41,42]. Using this technique, one can monitor luminescence profiles for materials with weak luminophores or low concentrations with well-defined bands, especially when both excitation and emission intensities are gathered as previously reported [41–43].

The degree of covalency between the metal ions and the organic sensor depends on the pH, and the linkage sites require tailoring the sensor under optimized conditions. For example, a study illustrated the solvent effect on the structural relaxation that follows the displacement of the electron cloud in the dipolar merocyanine dyes where variations were observed in the fluorescence quantum yield that is associated with the dielectric constant of the solvent. Specifically, using a series of solvents ordered by increasing dielectric constants, the optical gap was found to decrease as the polarity of the solvent increases, which resulted in the positive solvatochromic shift observed in the absorption and emission spectrum [44]. Therefore, all the SLS spectra recorded in this study represent analysis for solutions using similar aqueous compositions. Besides the high sensitivity and the low detection limit, SLS also helps to study changes that may occur during the process when new luminophores are formed during the binding processes under various pH buffer solutions and regular ambient water samples. Figure 2A shows the SLS spectra recorded at $\Delta\lambda = 50$ nm for **Sensor A** prepared in a water solution as well as adjusted pH buffer solutions. As shown in Figure 2, **Sensor A** has a strong luminescence band in the visible range along with two bands in the UV region at 275 and 325 nm indicating the presence of several luminophores. In addition, Figure 2B shows the UV-Vis absorption profiles recorded for **Sensor A** in various solvents. Both SLS and absorption profiles showed that the band that appears in the visible range is solvent- and pH-independent while the high-energy bands are pH- and solvent-dependent. This supports the fact that the low-energy band (visible region) is associated with the long chain of conjugation, while the high-energy modes are related to $n-\pi^*$ transitions that may be affected by varying solution pH in polar solvents. This provides both luminescent and colorimetric detection of the metal ions. The SLS spectra recorded under basic conditions showed a redshift in the high-energy bands compared to the analog spectra recorded at neutral and acidic conditions. This shift occurs because of the formation of a highly conjugated system obtained via the phenolate ions' formation.

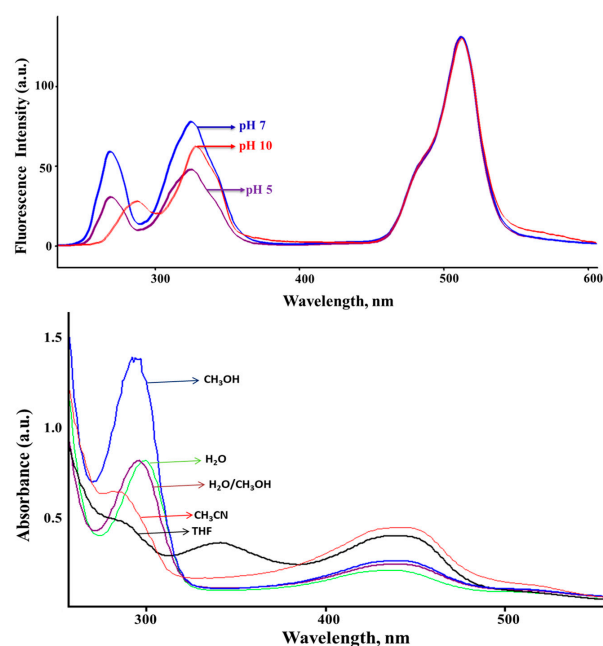


Figure 2. (A) Synchronous scan luminescence spectra recorded for **Sensor A** solutions at the indicated pH solutions as monitored at $\Delta\lambda = 50$ nm; (B) UV-Vis absorption spectra recorded for **Sensor A** prepared in various solvents as labeled.

To evaluate the quantum yield for **Sensor A**, we prepared known concentrations for **Sensor A** and fluorescein using methanol as a solvent. Using the absorption profile, the molar absorptivity for each solution was measured and found to be 2.335×10^5 and 3.96×10^5 L/mol cm, respectively. The integrated luminescence peak area for each solution was calculated using GRAMS software, and using the reported quantum yield value for the standard, we applied Equation (1) to calculate Φ_s for **Sensor A**. The calculated value was found to be 0.365.

Since our goal was to find a selective and sensitive sensor for the detection of specific metal ions in water bodies, the photophysical properties of **Sensor A** toward various concentrations of metal ions, including Hg^{2+} , Mg^{2+} , Na^+ , Zn^{2+} , Ni^{2+} , Pb^{2+} , Fe^{3+} , and Ca^{2+} ions, were investigated in various aqueous solutions adjusted at three different pH values (pH 5, 7, and 10). To test the ability of **Sensor A** as a luminescent sensor for the given target metal ion, its SLS spectrum was monitored as the metal ion concentration increased in the solution. In brief, SLS spectra were first recorded for 2.75 mL of 30 ppm solution of **Sensor A** mixed with 0.25 mL of water, and the obtained intensity was taken as a reference (F^0). Then, 2.75 mL of the sensor solution was mixed with 0.25 mL of various concentrations of the target metal ion, and the SLS spectra were recorded (referred to as F). To test the time required for complete binding (if any) between **Sensor A** and the target metal ion, we monitored the emission intensity of **Sensor A** combined with each metal ion for 15 min. Interestingly, an immediate response occurred with mercury and iron ions (within 30 s), and no response was observed for the other metal ions even at higher exposure time. Repeating the measurements for various concentrations, it was noticed that the sensor provides responses in a short time where the luminescence intensity is stabilized immediately upon mixing. However, in the testing protocol followed herein, all solutions were mixed for 2 min, after which the SLS spectra were recorded to obtain stable and consistent results.

Sensor A shows an immediate and strong response to both mercury and iron ions with no changes occurring for all other tested metal ions, including Na^+ , Mg^{2+} , Ca^{2+} , Ni^{2+} , Pb^{2+} , and Zn^{2+} . This is proved by the clear significant changes in the luminescence bands of **Sensor A** before and after the addition of various concentrations of mercury and iron ions. Figure 3 shows the SLS of **Sensor A** before and after adding various concentrations

of mercury ions as monitored at pH 5.0. As shown in Figure 3, the luminescence band intensities are gradually reduced when higher concentrations of mercury ions are added, with the quenching magnitude found to be directly proportional to the concentration of the quencher Hg^{2+} . As presented in Figure 3, a complete quenching for the band at 515 nm occurred at a 100 ppm Hg^{2+} concentration level (see Figure S1B for a full 2D scan after the addition of mercuric ions). Similarly, the emission intensity was quenched when different concentrations of Fe^{3+} were adequately mixed with Sensor A. As presented in Figure 4, the initial emission intensity at 510 nm tended to decrease when various levels of ferric ions were added, with complete quenching occurring at a 1000 ppm metal ion concentration. The conjugated probe tends to react with the target metal ion through the suitable donor sites affecting the electron cloud distribution of the sensor, thereby changing the output of the emission intensity of the starting material. Therefore, the results presented in Figures 3 and 4 indicate the high affinity of **Sensor A** for capturing mercury and iron ions from solutions, forming five-membered chelating rings through complexation with the probe via the imidazole nitrogen atom, pyridine nitrogen atom, and phenolic oxygen atom (Scheme 4). In contrast, the addition of other metal ions resulted in no clear changes in the emission profile of Sensor A, and thus no response toward these metal ions was detected (see examples presented in Figures S3–S5).

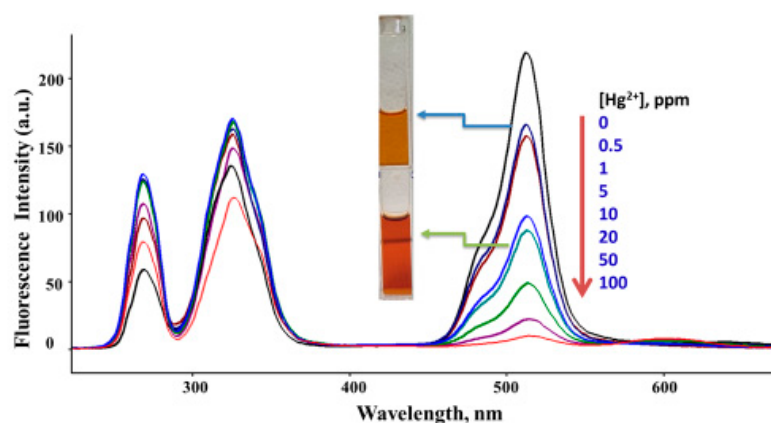


Figure 3. Synchronous scan luminescence spectra of **Sensor A** before and after adding various concentrations of mercury ions recorded at $\Delta\lambda$ of 50 nm and at pH = 5. The color represents **Sensor A** (top) and **Sensor A** mixed with 0.25 mL of 10 ppm Hg^{2+} solution (bottom).

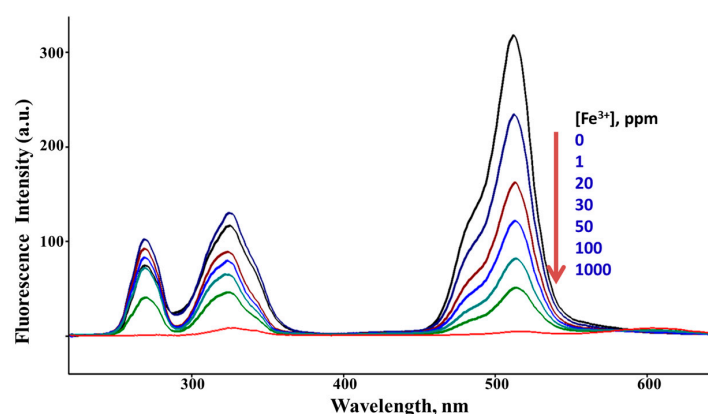
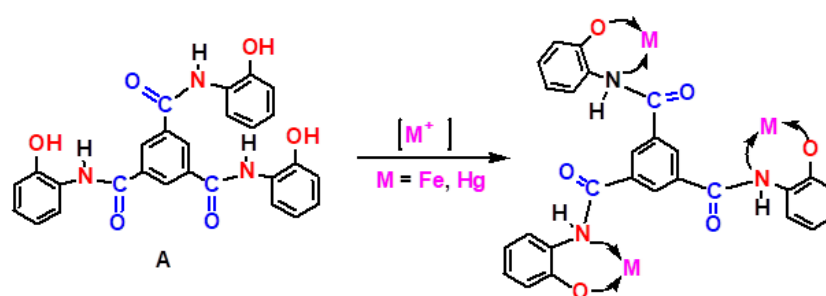


Figure 4. Synchronous scan luminescence spectra of **Sensor A** before and after adding various concentrations of Fe^{3+} ions recorded at $\Delta\lambda$ of 50 nm and at pH = 5.



Scheme 4. Binding model between **Sensor A** and the depicted metal ions.

FTIR spectroscopy is a powerful technique for identifying the mode of interaction between a given nucleophile and the metal surfaces. Given that the ligand–metal binding interaction involves changes in the electronic density and the bond strength of the ligand, one can identify the active modes associated with the metal surfaces and the ligand molecules using the FTIR technique. For example, pyridine is one of the common molecules used to probe the Lewis sites present in metal oxide surfaces. We have previously reported several studies with FTIR being used to identify surface acidic sites and the ligand interaction modes that include P-based molecules, pyridine, and various amine derivatives [45–49]. Given that the absorption modes of the C=N and C=C in pyridine are sensitive to the strength of the adsorption affinity, FTIR can identify the acidic sites based on the shifts associated with the C=N and C=C frequencies. Therefore, we used FT-ATR spectroscopy to monitor the changes that occurred between the starting material, **Sensor A**, and the sensor binding to metal ions. Figure 5 shows the FT-ATR spectra for trimesic acid and **Sensor A** before and after binding to 50 ppm mercury ion solution (after removal of the solvent). Trimesic acid showed bands in the range of 1105, 1250, and 1272 cm^{-1} assigned to the aromatic C-H in-plane bending vibrations. The bands that appear at 690, 740, and 990 cm^{-1} are assigned to the C-H out-of-plane bending modes. The characteristic infrared absorption bands of C=O appear at 1691 and 1713 cm^{-1} . The ring C=C stretching modes are observed at 1453 and 1604 cm^{-1} . Compared to the bands observed for trimesic acid, **Sensor A** shows stretching bands at 3303 and 3373 cm^{-1} assigned to the N-H stretching mode. The presence of the C=O mode at 1690 cm^{-1} along with the C=C and C=N modes appear at 1460 and 1498 cm^{-1} , supporting the formation of the amide moieties. After the binding to mercury ions, bands were observed at 1627 and 1468, along with a broad band centered at 1313 cm^{-1} . The C=N and C=O modes were shifted to appear at 1627 cm^{-1} , supporting their binding to mercury ions that weakened the C=O and C-N modes (Scheme 4).

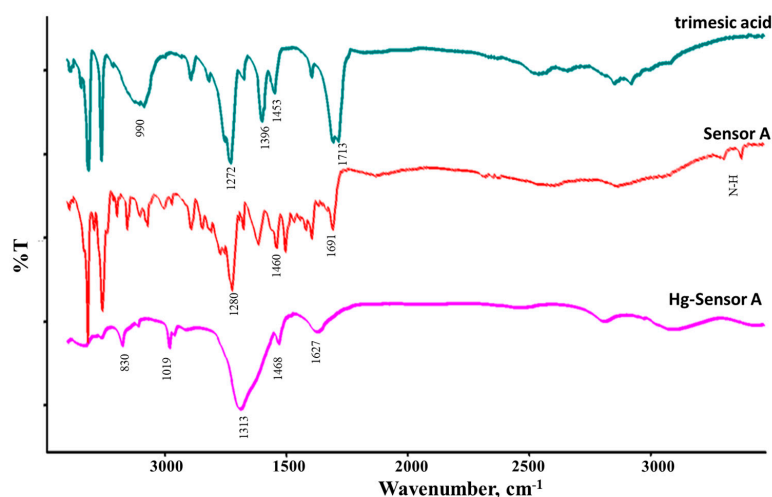


Figure 5. FT-ATR spectra for trimesic acid, **Sensor A**, and Hg^{2+} bound to **Sensor A**.

Luminescence quenching resulting from the collision between the emitting moiety and the quencher is described as a dynamic quenching. In such a process, the kinetics is described quantitatively by the Stern–Vomer equation evidenced by a linear dependence of Φ_0/Φ from the concentration of the quencher in homogeneous solvents:

$$\Phi_0/\Phi = \tau_0/\tau = 1 + k_q\tau_0[Q] \quad (4)$$

where τ_0 and Φ_0 are the luminescence lifetime and quantum yield of the fluorophore in the same conditions without the quencher (Q). τ and Φ are the luminescence lifetime and quantum yield of the fluorophore in the presence of Q. k_q is the kinetic constant of the quenching process. Instead of measuring the quantum yield before and after the quencher, the ratio F^0/F can be simply used as presented in Equation (5) with the Stern–Volmer binding constant (K_{sv}) represented by the products of $k_q \times \tau_0$ [42,43].

$$F_0/F = 1 + K_{sv} [Q] \quad (5)$$

where $[Q]$ is the metal ion concentration (quencher), and F_0 and F represent the fluorescence intensity of the sensor before and after the quencher is added.

Figure 6 shows the Stern–Volmer plots that describe the affinity of the mercuric ions (Figure 6A) and ferric ions (Figure 6B) for reducing the initial emission intensity of the sensor upon mixing at various pHs. As shown in Figure 6, the plot provides a good correlation between the normalized emission intensity before and after various concentrations of Hg^{2+} and Fe^{3+} are added, and excellent correlations as determined by R^2 values are presented. This is expected given that more covalency occurred between the iron or mercury ions that are classified as soft acids and the intermediate basic sites represented via oxygen and imine nitrogen linkage. As presented in Figure 6A,B, the binding affinity of **Sensor A** to Hg^{2+} is 4 times higher than that observed for Fe^{3+} (Table 1). The binding affinity also tends to vary when the pH of the solution is varied using buffers at pH 7 and 10. The binding constants obtained for **Sensor A** at various pH conditions are presented in Figure 6 and summarized in Table 1. As depicted in Table 1, **Sensor A** has a strong binding affinity for both metal ions detected in acidic and neutral conditions.

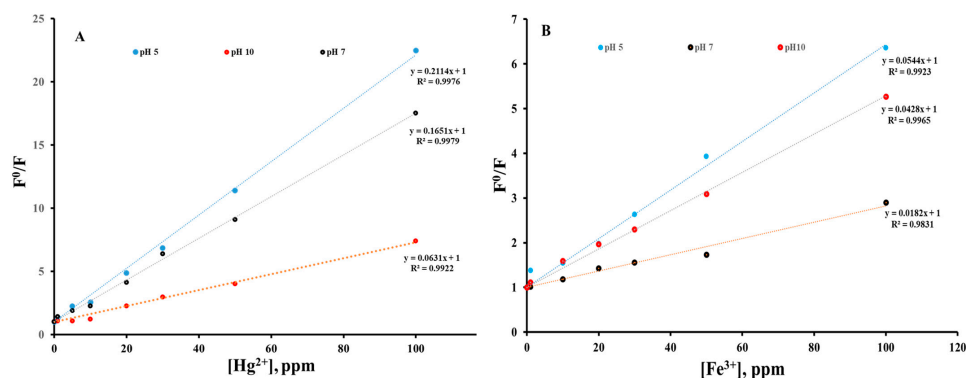


Figure 6. The Stern–Volmer plots of **Sensor A** binding to various concentrations monitored in different pH solutions for (A) Hg^{2+} and (B) Fe^{3+} .

Table 1. A summary of the calculated binding affinities (K_{sv}) between **Sensor A** and mercury and iron ions at various pH conditions.

	pH 5	pH 7	pH 10
$K_{sv} Hg^{2+}/\text{Sensor A}$	0.2114	0.1650	0.0631
$K_{sv} Fe^{3+}/\text{Sensor A}$	0.0544	0.0184	0.0428
$K_{sv} Hg^{2+}/K_{sv} Fe^{3+}$	3.89	8.97	1.47

The response toward Hg^{2+} was linear in the concentration range of 50 ppb to 100 ppm with a limit of detection of 2 ppb. In addition, **Sensor A** showed a wide linear response in the range of 10 ppb to 1000 ppm toward iron ions. This is very important for detecting low levels of Fe^{3+} in an aqueous medium at the nanomolar scale since Fe^{3+} is considered among the most important metal ions in biological systems and exerts an incomparable role in many biological processes, including RNA and DNA synthesis and metabolism. While the sensor showed a good response toward both mercury and iron ions, the binding affinity was found to vary at a given pH condition. For example, the relative binding affinity of **Sensor A** with mercury ions to that of iron ions is 1.5 at pH 10. This affinity increased to around 4- and 9-fold under acidic and neutral conditions, respectively. The strong binding with mercury is expected due to its preference to bind to N-based donor ligands, especially those associated with aromatic and conjugated systems as presented herein. The sensor also provides a special skeletal arrangement that allows good size fitting to capture large metal ions under all pH conditions employed (Scheme 4).

To explore selectivity, in two separate experiments, Sensor A was exposed to 50 ppm mercuric ion solution in one trial. In a separate trial, Sensor A was exposed to a mixture of all ions (including Hg^{2+}). Figure 7 shows the SLS for Sensor A alone and after mercuric ions were added to A as well as a mixture containing 50 ppm of each ion implemented in this study. Interestingly, the response of Sensor A to mercuric ions was almost equivalent to the response obtained for the mixture solution. This indicates that Sensor A can exhibit selective detection of mercuric ions in environmental water samples (see Figure S6).

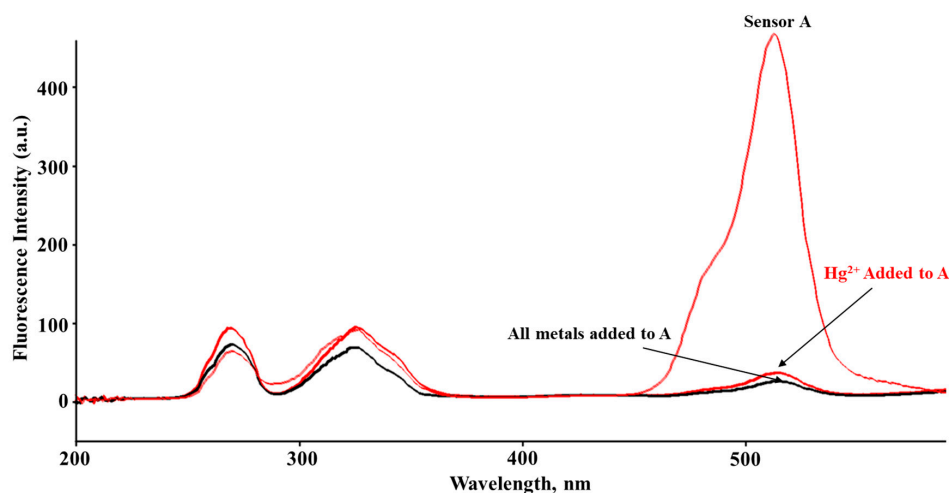


Figure 7. SLS of Sensor A, mercuric ion added to A, and mixed ions added to A.

For the potential use of **Sensor A** for real water samples, we tested several environmental, tap, and deionized water samples. Further, tap water samples contaminated with 50 ppm iron and mercury ions in isolated and mixture forms were also evaluated. The SLS of **Sensor A** was not affected by the addition of deionized water. The tap water showed a slight reduction in the synchronous scan luminescence bands estimating the iron level to the level of a few ppm, which was confirmed by ICP analysis. The spiked water samples were added in a different sequence. When 0.25 mL of the sample spiked with 50 ppm iron ions was mixed with **Sensor A**, the emission intensity was reduced by 65%, with this reduction reaching 97% when the same volume of a water sample spiked with 50 ppm mercury ions was added. Similarly, when a sample spiked with mixed ions or with mercury ions alone was used, a direct quenching occurred with above 95% reduction in the initial emission intensity observed (see Figure S7). To evaluate the sensor response to real water samples, we used three various dilutions of spiked mercuric ions and monitored the adsorbed levels using luminescent and ICP-OES spectroscopic methods. Table 2 summarizes the spiked concentrations and the adsorbed concentration levels as depicted in both techniques. As shown in Table 2, when low concentrations were applied, no mercuric

concentrations were detected using ICP, whereas the use of higher mercuric levels provided an excess amount in ICP detection with 94.2% adsorption occurring. This supports the results presented in Table 1 showing that the sensor provides a high binding affinity toward mercury ions compared to iron ions. Compared to previous studies, **Sensor A** provides a low detection limit towards mercury in a short period of time, and it can be applied for environmental sample analysis based on its water solubility. Table 3 summarizes the major detection features obtained for Sensor A and compares Sensor A to other sensors reported for mercuric ion detection.

Table 2. Analysis of Hg^{2+} spiked in tap water samples using luminescence and ICP techniques.

V (mL) of 50 ppm Hg^{2+} Added	$[\text{Hg}^{2+}]$, ppm Spiked in the Final Solution	$[\text{Hg}^{2+}]$, ppm Adsorbed Luminescence Detection	% $[\text{Hg}^{2+}]$ Adsorbed Luminescence Detection	% $[\text{Hg}^{2+}]$ Adsorbed ICP-OES Detection
0.6	11.5	11.36	98.78	100
1.5	21.4	20.60	96.26	100
3.5	34.7	32.13	92.60	94.2

Table 3. Comparative results between Sensor A and previous results reported for Hg^{2+} detection.

Sensing Platform	LoD	Working Media	Detection Time	Ref.
Sensor A	50 ppb	10:90 <i>v:v</i> methanol–water	<30 s	This study
Aminal-linked POPs	—	suspension in water	30 min	[50]
ss-DNA-GO	0.92 nM	water	5 min	[51]
Iminodiacetate-based Tb(III) cyclen	3.26 nM	water detects Cu^{2+} and Hg^{2+}	–	[52]
Iridium(III) complex-mediated AgNPs	5 nM	water	Selective detection in short time	[53]
Pyrene-based sensor	2ppb	DMF–water	96 h aging time	[54]
DNA hairpin probe–GO	0.3 nM	water	40 min	[55]

In summary, a highly conjugated organic molecule was synthesized in a one-step reaction using low-cost and safe starting materials. Besides its high solubility in polar solvents, the unique electronic and skeletal structures depicted by the orientation of the N- and O- provide multiple active sites that are suitable for attracting mercuric and ferric ions (Scheme 4) with low detection limits and wide linear detection range (micromolar to nanomolar), thus enabling a wide range of applications to biological and environmental samples. Further, Sensor A is a highly conjugated organic framework that provides both colorimetric and fluorometric signatures when it covalently binds to the target metal ions. It was shown that both the emission intensity and the color of the dye immediately changed upon being mixed with mercuric ions (less than 30 s). Finally, the material was tested for detection of mercuric and ferric ions in real water samples and showed high affinity for adsorbing mercuric ions from water bodies with the measured adsorption capacity of 1.2–2.0 mg/g, and the removal efficiency from water samples reached 98.8% at pH 7.0.

4. Conclusions

The prepared substrate, N^1, N^3, N^5 -tris(2-hydroxyphenyl)benzene-1,3,5-tricarboxamide, was found to be a good substrate to capture mercury(II) and iron(III) contaminants in water samples. Sensor A showed strong luminescent profiles that are sensitive toward trace concentrations of mercury and iron ions under neutral, acidic, and basic conditions. The binding affinity toward mercury ions was always higher than that observed for iron ions under similar conditions. Given that the sensor– Hg^{2+} interaction was found to be best at a pH value range of 5.0–7.0, the sensor fabricated is a good substrate for mercuric ion detection at ambient environmental conditions. The affinity of **Sensor A** for binding to Hg^{2+} at pH 7 is almost 9 times higher than its binding affinity toward iron ions. No clear binding was detected between **Sensor A** and other metal ions that are present in water bodies, including sodium, potassium, and magnesium ions.

Supplementary Materials: The following supporting information can be downloaded at: <https://www.mdpi.com/article/10.3390/chemosensors11050308/s1>, Figure S1. 2D full range excitation and emission profiles for (A) Sensor A solution alone and (B) Sensor A solution in the presence of 100 ppm Hg^{2+} solution at pH 5. Figure S2. EI-Mass spectrum for Sensor A. Figure S3: SSLS of Sensor A before and after adding various concentrations of sodium ion. Figure S4: SSLS of Sensor A before and after adding various concentrations of Zinc ion. Figure S5: SSLS of Sensor A before and after adding various concentrations of Magnesium ion. Figure S6. Synchronous Scan Luminescence Spectra of Sensor A before and after adding various concentrations of mercury ions recorded at $\Delta\lambda$ of 50 nm and at pH = 7. Figure S7: SSLS of Sensor A before and after sequential addition of 50 ppm ferric ion and mercuric ion solutions spiked into tap water samples at pH 7.

Author Contributions: All authors contributed to the study conception and design. Material preparation and data collection and analysis were performed by all authors. The first draft of the manuscript was written by S.K. and all authors commented on previous versions of the manuscript. All authors have read and agreed to the published version of the manuscript.

Funding: This work was funded by the Research Office at the American University of Sharjah Grant Number FRG22-C-S77. This research received no external funding.

Institutional Review Board Statement: Not applicable.

Informed Consent Statement: Not applicable.

Data Availability Statement: Not applicable.

Conflicts of Interest: The authors have no relevant financial or non-financial interests to disclose.

References

1. Renzoni, A.; Zino, F.; Franchi, E. Mercury levels along the food chain and risk for exposed populations. *Environ. Res.* **1998**, *77*, 68–72. [[CrossRef](#)] [[PubMed](#)]
2. He, L.; Wang, S.; Liu, M.; Chen, Z.; Xu, J.; Dong, Y. Transport and transformation of atmospheric metals in ecosystems: A review. *J. Hazard. Mater. Adv.* **2023**, *9*, 100218. [[CrossRef](#)]
3. Mng'Ong'O, M.; Munishi, L.K.; Ndakidemi, P.A.; Blake, W.; Comber, S.; Hutchinson, T.H. Toxic metals in East African agro-ecosystems: Key risks for sustainable food production. *J. Environ. Manag.* **2021**, *294*, 112973. [[CrossRef](#)] [[PubMed](#)]
4. Zhang, H.; Zhao, Y.; Wang, Z.; Liu, Y. Distribution characteristics, bioaccumulation and trophic transfer of heavy metals in the food web of grassland ecosystems. *Chemosphere* **2021**, *278*, 130407. [[CrossRef](#)]
5. Cheng, H.F.; Hu, Y.A. Lead (Pb) Isotopic Fingerprinting and Its Applications in Lead Pollution Studies in China: A Review. *Environ. Pollut.* **2009**, *58*, 1134–1146. [[CrossRef](#)]
6. Di Bella, C.; Calagna, A.; Cammilleri, G.; Schembri, P.; Monaco, D.L.; Cipri, V.; Battaglia, L.; Barbera, G.; Ferrantelli, V.; Sadok, S.; et al. Risk assessment of cadmium, lead, and mercury on human health in relation to the consumption of farmed sea bass in Italy: A meta-analytical approach. *Front. Mar. Sci.* **2021**, *8*, 616488. [[CrossRef](#)]
7. Panhwar, A.H.; Kazi, T.G.; Afridi, H.I.; Arain, S.A.; Arain, M.S.; Brahaman, K.D.; Naeemullah, A.S. Correlation of cadmium and aluminum in blood samples of kidney disorder patients with drinking water and tobacco smoking: Related health risk. *Geochem. Health* **2016**, *38*, 265–274. [[CrossRef](#)]
8. Tong, S.Y.; Meija, J.; Zhou, L.; Methven, B.; Mester, Z.; Yang, L. High-precision measurements of the isotopic composition of common lead using MC-ICPMS: Comparison of calibration strategies based on full gravimetric isotope mixture and regression models. *Anal. Chem.* **2019**, *91*, 4164–4171. [[CrossRef](#)]

9. Luo, X.; Liu, L.; Deng, F.; Luo, S. Novel ion-imprinted polymer using crown ether as a functional monomer for selective removal of pb(ii) ions in real environmental water samples. *J. Mater. Chem. A* **2013**, *1*, 8280–8286. [[CrossRef](#)]
10. Wani, A.B.; Ara, A.; Usmani, J.A. Lead Toxicity: A Review. *Interdiscip. Toxicol.* **2015**, *8*, 55–64. [[CrossRef](#)]
11. Charvát, P.; Klimeš, K.; Pospíšil, J.; Klemeš, J.; Varbanov, P. An overview of mercury emissions in the energy industry—A step to mercury footprint assessment. *J. Clean. Prod.* **2020**, *267*, 122087. [[CrossRef](#)]
12. Dworak, S.; Rechberger, H. Mercury throughput of the Austrian manufacturing industry—Discussion of data and data gaps. Resources. *Conserv. Recycl.* **2021**, *166*, 105344. [[CrossRef](#)]
13. Dziok, T.; Bury, M.; Burmistrz, P. Mercury release from municipal solid waste in the thermal treatment process. *Fuel* **2022**, *329*, 125528. [[CrossRef](#)]
14. Sun, W.; Wang, Q.; Zhou, Y.; Wu, J. Material and energy flows of the iron and steel industry: Status quo, challenges and perspectives. *Appl. Energy* **2020**, *268*, 114946. [[CrossRef](#)]
15. Xin, H.; Wang, S.; Chun, T.; Xue, X.; Long, W.; Xue, R.; Zhang, R. Effective pathways for energy conservation and emission reduction in iron and steel industry towards peaking carbon emissions in China: Case study of Henan. *J. Clean. Prod.* **2023**, *399*, 136637. [[CrossRef](#)]
16. Zhang, X.; Xue, C.; Wang, R.; Shen, R.; Lan, P. Physiological and proteomic dissection of the rice roots in response to iron deficiency and excess. *J. Proteom.* **2022**, *267*, 2022. [[CrossRef](#)]
17. Guo, L.; Wu, P.; Jiang, W.; Liu, Y.; Kuang, S.; Jiang, J.; Tang, L.; Tang, W.; Zhang, Y.; Zhou, Q.; et al. The impaired immune function and structural integrity by dietary iron deficiency or excess in gill of fish after infection with *Flavobacterium columnare*: Regulation of NF- κ B, TOR, JNK, p38MAPK, Nrf2 and MLCK signaling. *Fish Shellfish Immunol.* **2018**, *74*, 593–608. [[CrossRef](#)]
18. Perng, V.; Li, C.; Navazesh, S.; Klocke, C.; Pinneles, D.; Lein, P.; Ji, P. Iron Deficiency and Iron Excess Alter Dendritic Architecture of Pyramidal Neurons in the Hippocampus of Neonatal Pigs. *Curr. Dev. Nutr.* **2020**, *4*, 4141232. [[CrossRef](#)]
19. World Health Organization. *Guidelines for Drinking-Water Quality: Recommendations*; World Health Organization: Geneva, Switzerland, 2004.
20. Volynkin, S.S.; Demakov, P.A.; Shuvaeva, O.V.; Kovalenko, K.A. Metal-organic framework application for mercury speciation using solid phase extraction followed by direct thermal release–electrothermal atomization atomic absorption spectrophotometric detection (ETA AAS). *Anal. Chim. Acta* **2021**, *1177*, 338795. [[CrossRef](#)]
21. dos Santos, N.; dos Santos, L.; Damin, I.; Vale, M.; Dessuy, M. Multielement determination of metals in edible seeds by HR-CS GF AAS and direct analysis. *J. Food Compos. Anal.* **2022**, *111*, 104625. [[CrossRef](#)]
22. Lores-Padín, A.; Fernández, B.; García, M.; González-Iglesias, H.; Pereiro, R. Real matrix-matched standards for quantitative bioimaging of cytosolic proteins in individual cells using metal nanoclusters as immunoprobes-label: A case study using laser ablation ICP-MS detection. *Anal. Chim. Acta* **2022**, *1221*, 340128. [[CrossRef](#)]
23. Qin, J.; Su, Z.; Mao, Y.; Liu, C.; Qi, B.; Fang, G.; Wang, S. Carboxyl-functionalized hollow polymer microspheres for detection of trace metal elements in complex food matrixes by ICP-MS assisted with solid-phase extraction. *Ecotoxicol. Environ. Saf.* **2021**, *208*, 111729. [[CrossRef](#)]
24. Dimpe, K.; Ngila, J.; Mabuba, N.; Nomngongo, P. Evaluation of sample preparation methods for the detection of total metal content using inductively coupled plasma optical emission spectrometry (ICP-OES) in wastewater and sludge. *Phys. Chem. Earth Parts A/B/C* **2014**, *76–78*, 42–48. [[CrossRef](#)]
25. Pal, H.; Majumder, S. Ultra-low-level detection of mercury (Hg²⁺) heavy metal carcinogens in aqueous medium using electrochemistry. *Mater. Today Proc.* **2020**, *29*, 1129–1131. [[CrossRef](#)]
26. Tong, Y.; Wu, Y.; Bai, H.; Li, S.; Jiang, L.; Zhou, Q.; Chen, C. Highly efficient and simultaneous magnetic solid phase extraction of heavy metal ions from water samples with L-cysteine modified magnetic polyamidoamine dendrimers prior to high performance liquid chromatography. *Chemosphere* **2023**, *313*, 137340. [[CrossRef](#)]
27. Dehdashtian, S.; Pourreza, N.; Rostamnia, S. Electrochemical sensing of indole in plasma using Pd nanoparticles modified metal-organic framework Cr-MIL-101/ionic liquid sensor. *Microchem. J.* **2022**, *181*, 107839. [[CrossRef](#)]
28. Darwish, N.; Kurdi, A.; Alshihri, S.; Tabbakh, T. Organic heterocyclic-based colorimetric and fluorimetric chemosensors for the detection of different analytes: A review (from 2015 to 2022). *Mater. Today Chem.* **2023**, *27*, 101347. [[CrossRef](#)]
29. Li, A.; Liu, Y.; Chen, Z.; Li, S.; Zhong, R.; Cheng, D.; Chen, L.; He, L. Development of a Golgi-targeted fluorescent chemosensor for detecting ferrous ions overload under Golgi stress. *Spectrochim. Acta Part A: Mol. Biomol. Spectrosc.* **2023**, *294*, 122560. [[CrossRef](#)]
30. Pandey, H.P.; Aggarwal, S.; Vats, M.; Rawat, V.; Pathak, S. Coumarin-based Chemosensors for Metal Ions Detection. *Asian J. Org. Chem.* **2022**, *11*, 23–75. [[CrossRef](#)]
31. Kanan, S.; Abu-Yousef, I.; Hassouneh, N.; Malkawi, A.; Abdo, N.; Kanan, M. A Highly Selective Luminescent Sensor for Detecting Mercuric Ions in Water. *Aust. J. Chem.* **2019**, *62*, 1593–1599. [[CrossRef](#)]
32. Rasin, P.; Haribabu, J.; Malappuram, K.; Manakkadan, V.; Palakkeezhillam, V.N.; Cesar Echeverria, C.; Sreekanth, A. A “turn-on” fluorescent chemosensor for the meticulous detection of gallium (III) ion and its use in live cell imaging, logic gates and keypad locks. *J. Photochem. Photobiol. A Chem.* **2023**, *437*, 114493. [[CrossRef](#)]
33. Xie, H.; Hu, Q.; Qin, X.; Zhang, Y.; Li, L.; Li, J. Naked-eye chemosensor with high absolute fluorescence quantum yield for selective detection of Cu(II) and cell imaging. *Spectrochim. Acta Part A Mol. Biomol. Spectrosc.* **2022**, *283*, 121740. [[CrossRef](#)] [[PubMed](#)]

34. Kanan, S.; Malkawi, A. Recent advances in nanocomposite luminescent metal-organic framework sensors for detecting metal ions. *Comments Inorg. Chem.* **2021**, *41*, 1–66. [[CrossRef](#)]
35. Jiang, J.; Lu, Y.; Zhou, Y.; Zhao, D.; Li, C. An Acid-base Resistant Zn-based Metal-organic Framework as a Luminescent Sensor for mercury(II). *J. Solid State Chem.* **2020**, *283*, 121–153. [[CrossRef](#)]
36. Kang, W.; Han, C.; Liu, D.; Cui, G. A Bifunctional Benzimidazole-based Luminescent Zn²⁺ Coordination Polymer for Detection of Hg²⁺ and Photocatalytic Degrading of Methylene Blue. *Inorg. Chem. Commun.* **2019**, *106*, 81–85. [[CrossRef](#)]
37. Wan, Y.; Zou, D.; Cui, Y.; Yang, Y.; Qian, G. A Zn Based Anionic Metal-organic Framework for Trace Hg²⁺ Ion Detection. *J. Solid State Chem.* **2018**, *266*, 70–73. [[CrossRef](#)]
38. Latt, K.K.; Takahashi, Y. Fabrication and characterization of a $\alpha,\beta,\gamma,\delta$ -Tetrakis(1-methylpyridinium-4-yl)porphine/silica nanocomposite thin-layer membrane for detection of ppb-level heavy metal ions. *Anal. Chim. Acta* **2011**, *689*, 103–109. [[CrossRef](#)]
39. Yang, Y.; Jiang, J.; Shen, G.; Yu, R. An optical sensor for mercury ion based on the fluorescence quenching of tetra(p-dimethylaminophenyl)porphyrin. *Anal. Chim. Acta* **2009**, *636*, 83–88. [[CrossRef](#)]
40. Jian, Y.; Zhe, W.; Li, Y.; Wenru, Q.; Jinlou, G. Porphyrinic MOFs for reversible fluorescent and colorimetric sensing of mercury(ii) ions in aqueous phase. *RSC Adv.* **2016**, *6*, 69807–69814.
41. Kanan, S.; Kanan, M.; Patterson, H. Silver nanoclusters doped in X and mordenite zeolites as heterogeneous catalysts for the decomposition of carbamate pesticides in solution. *Res. Chem. Intermed.* **2006**, *32*, 871. [[CrossRef](#)]
42. Kanan, S.; Kanan, M.; Patterson, H. Photoluminescence spectroscopy as a probe of silver doped zeolites as photocatalysts. *Curr. Opin. Solid State Mater. Sci.* **2003**, *7*, 443. [[CrossRef](#)]
43. Fan, J.; Peng, Y.; Wu, E.; Lu, J.; Hou, J.; Zhang, H.; Zhang, R.; Fu, X. A new PET fluorescent sensor for Zn²⁺. *J. Lumin.* **2005**, *114*, 125. [[CrossRef](#)]
44. Hoche, J.; Schulz, A.; Fietrich, L. The origin of the solvent dependence of fluorescence quantum yields in dipolar merocyanine dyes. *Chem. Sci.* **2019**, *10*, 11013. [[CrossRef](#)] [[PubMed](#)]
45. El-Sayed, Y.; Abu-Farha, N.; Kanan, S. Synthesis and characterization of porous WO₃-SnO₂ nanomaterials: An infrared study of adsorbed pyridine and dimethyl methylphosphonate. *Vib. Spectrosc.* **2014**, *75*, 78–85. [[CrossRef](#)]
46. Kanan, S.M.; Tripp, C.P. Synthesis, FTIR Studies and Sensor properties of WO₃ powders. *Curr. Opin. Solid State Mater. Sci.* **2007**, *11*, 19–27. [[CrossRef](#)]
47. Waghe, A.; Kanan, S.M.; Abu-Yousef, I.A.; Jensen, B.; Tripp, C.P. Infrared study of uv irradiated tungsten trioxide powders containing adsorbed dimethyl methyl phosphonate and trimethyl phosphate. *Res. Chem. Int.* **2006**, *32*, 613–623. [[CrossRef](#)]
48. Kanan, S.M.; Lu, Z.; Cox, J.K.; Bernhardt, G.; Tripp, C.P. Identification of Surface Sites on Monoclinic WO₃ Powders by Infrared Spectroscopy. *Langmuir* **2002**, *18*, 1707–1712. [[CrossRef](#)]
49. Abla, F.; Elsayed, Y.; Abu Farha, N.; Obaideen, K.; Mohamed, A.A.; Lee, H.; Han, C.; Egilmez, M.; Kanan, S. Fabrication of high surface area tio₂-moo₃ nanocomposite as a photocatalyst for organic pollutants removal from water bodies. *Catalysts* **2023**, *13*, 362. [[CrossRef](#)]
50. Sabri, M.A.; Al-Sayah, M.H.; Sen, S.; Ibrahim, T.H.; El-Kadri, O.M. Fluorescent aminal linked porous organic polymer for reversible iodine capture and sensing. *Sci. Rep.* **2020**, *10*, 15943. [[CrossRef](#)]
51. Li, M.; Zhou, X.; Ding, W.; Guo, S.; Wu, N. Fluorescent aptamer-functionalized graphene oxide biosensor for label-free detection of mercury(II). *Biosens. Bioelectron.* **2013**, *41*, 889–893. [[CrossRef](#)] [[PubMed](#)]
52. Brian, K.; Thorfinnur, G. Lanthanide luminescence sensing of copper and mercury ions using an iminodiacetate based Tb(III)-cyclen chemosensor. *Tetrahedron Lett.* **2010**, *51*, 5406–5410.
53. Liu, J.; Vellaisamy, K.; Yang, G.; Leung, C.-H.; Ma, D.-L. Luminescent turn-on detection of Hg(II) via the quenching of an iridium(III) complex by Hg(II)-mediated silver nanoparticles. *Sci. Rep.* **2017**, *7*, 3620. [[CrossRef](#)] [[PubMed](#)]
54. Zeynep, M.; Dilek, A.; Magdalena, M.; Muhammet, E.; Faruk, Y. Highly sensitive and reusable mercury (II) sensor based on fluorescence quenching of pyrene moiety in polyacrylamide-based cryogel. *Sens. Actuators B Chem.* **2017**, *242*, 362–368. [[CrossRef](#)]
55. Huang, J.; Gao, X.; Jia, J.; Kim, J.; Li, Z. Graphene oxide-based amplified fluorescent biosensor for Hg(2+) detection through hybridization chain reactions. *Anal. Chem.* **2014**, *86*, 3209–3215. [[CrossRef](#)] [[PubMed](#)]

Disclaimer/Publisher's Note: The statements, opinions and data contained in all publications are solely those of the individual author(s) and contributor(s) and not of MDPI and/or the editor(s). MDPI and/or the editor(s) disclaim responsibility for any injury to people or property resulting from any ideas, methods, instructions or products referred to in the content.